Environmental Science & Technology

Article

pubs.acs.org/est

Single Silver Adatoms on Nanostructured Manganese Oxide Surfaces: Boosting Oxygen Activation for Benzene Abatement

Yaxin Chen,[†] Zhiwei Huang,[†] Meijuan Zhou,[†] Zhen Ma,[†] Jianmin Chen,[†] and Xingfu Tang*[,†,‡]

[†]Institute of Atmospheric Sciences, Shanghai Key Laboratory of Atmospheric Particle Pollution and Prevention (LAP[3]), Department of Environmental Science and Engineering, Fudan University, Shanghai 200433, China

[‡]Jiangsu Collaborative Innovation Center of Atmospheric Environment and Equipment Technology (CICAEET), Nanjing University of Information Science and Technology, Nanjing, Jiangsu 210044, China

Supporting Information

ABSTRACT: The involvement of a great amount of active oxygen species is a crucial requirement for catalytic oxidation of benzene, because complete mineralization of one benzene molecule needs 15 oxygen atoms. Here, we disperse single silver adatoms on nanostructured hollandite manganese oxide (HMO) surfaces by using a thermal diffusion method. The single-atom silver catalyst (Ag_1/HMO) shows high catalytic activity in benzene oxidation, and 100% conversion is achieved at 220 °C at a high space velocity of 23 000 h^{-1}. The Mars-van Krevelen mechanism is valid in our case as the reaction orders for both benzene and O_2 approach one, according to reaction kinetics data. Data from H_2 temperature-programmed reduction and O core-level X-ray photoelectron spectra (XPS) reveal that Ag_1/HMO possesses a great amount of active surface lattice oxygen available for benzene oxidation. Valence-band XPS and density functional theoretical calculations demonstrate that the single Ag adatoms have the upshifted 4*d* orbitals, thus facilitating the activation of gaseous oxygen. Therefore, the excellent activation abilities of Ag_1/HMO toward both surface lattice oxygen and gaseous oxygen account for its high catalytic activity in benzene oxidation. This work may assist with the rational design of efficient metal-oxide catalysts for the abatement of volatile organic compounds such as benzene.

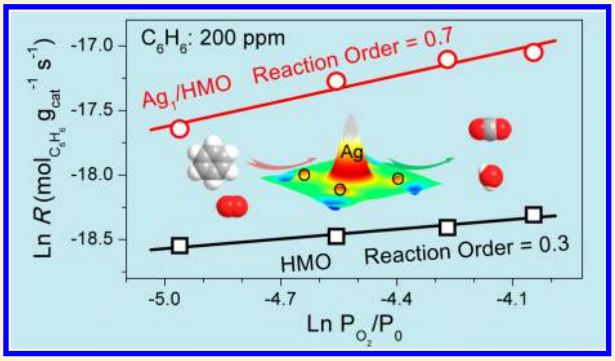

INTRODUCTION

Benzene, widely used as an industrial solvent, an intermediate in chemical synthesis, and a component of gasoline,[1,2] is one of the typical volatile organic compounds (VOCs). It has a detrimental effect on both human health and the atmospheric environment.[3−5] The U.S. Environmental Protection Agency has classified benzene into known human carcinogens.[3] Furthermore, benzene can contribute to the formation of secondary organic aerosol.[4,5] Therefore, great effort has been made to control benzene emission.

Catalytic oxidation is one of the most promising technologies for complete oxidation of gas-phase benzene to CO_2 and H_2O.[6,7] Catalysts used for the oxidation of benzene include supported noble metals[8−10] and transition metal oxides.[11−15] A key requirement is that a catalyst should be effective in activating both lattice oxygen and O_2 required for the reaction $C_6H_6 + 7.5O_2 \rightarrow 6CO_2 + 3H_2O$, because benzene oxidation is known to follow the Mar-van Krevelen (M-K) mechanism in many cases.[7,12,16] These activated oxygen species are favorable for cleaving stable delocalized π bonds and strong C−H bonds of benzene.

The lattice oxygen of manganese oxides, typically hollandite manganese oxides (HMO), demonstrates high mobility and reactivity. Manganese oxides have been used for the oxidation of benzene,[7,11] toluene,[11,16,17] ethanol,[16,18] and formaldehyde.[19,20] It is well-known that silver (Ag) can adsorb and activate gaseous O_2, so that adsorbed active oxygen species can react with these pollutants.[21,22] Therefore, the combination of HMO and Ag to develop Ag/HMO catalysts should be favorable for the catalytic oxidation of VOCs. For instance, Ag/HMO showed excellent catalytic performance for ethanol oxidation,[23] because the O anions of the Ag−O−Mn bridging bonds are active and the Ag−O−Mn bridge facilitates a redox cycle by the electron transfer between Ag and Mn.[24] More interestingly, support nanostructures are favorable for enhancing catalytic activity by boosting electrons or oxygen transfer between metals and supports.[25−27] Hence, the utilization of nanostructured HMO supports to make Ag-based catalysts could improve the catalytic activity in the low-temperature oxidation of formaldehyde and CO,[26,27] due to strong activation abilities to both lattice oxygen and molecular oxygen.

In this work, we dispersed single Ag adatoms on nanostructured HMO surfaces (Ag_1/HMO) for the catalytic

Received: August 26, 2016
Revised: January 10, 2017
Accepted: January 19, 2017
Published: January 23, 2017

DOI: 10.1021/acs.est.6b04340
Environ. Sci. Technol. 2017, 51, 2304−2311

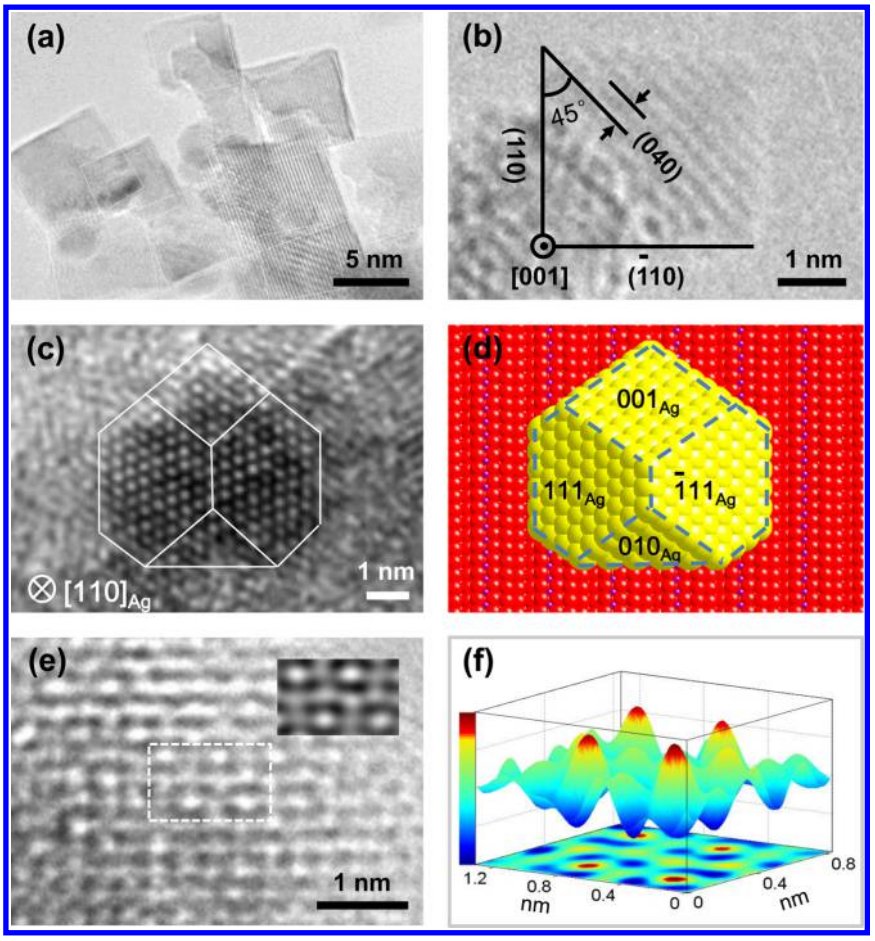

Figure 1. (a) TEM and (b) HRTEM images of HMO NPs. (c) HRTEM image and (d) the corresponding model of Ag_{NP}/HMO. Yellow, purple, and red balls represent Ag, Mn, and O atoms, respectively. Subscript "Ag" in panels (c,d) identifies the crystal facets or axis of Ag NPs. (e) HRTEM image of Ag_1/HMO. Inset: FT filtered HRTEM image in the dashed rectangle. (f) Two/three-dimensional images of the simulated image in panel (e) showing the difference of contrast between Ag, Mn, and the background.

oxidation of benzene. The geometric and electronic structures of surface Ag atoms were evidenced by electronic microscopy images and X-ray absorption spectra. The catalytic performance of Ag_1/HMO was evaluated at relatively low temperature. The structure−activity correlation in catalytic oxidation of benzene over Ag_1/HMO was also established by combining experimental data with theoretical calculations from the oxygen activation viewpoint.

EXPERIMENTAL SECTION

Material Preparation. HMO nanoparticles (NPs) were prepared by a hydrothermal route:[28] $KMnO_4$ (11.600 g, 73.6 mmol), Na_2MoO_4 (1.228 g, 5.2 mmol), $Na_3VO_4{\cdot}12H_2O$ (3.840 g, 9.6 mmol), and $TiOSO_4{\cdot}H_2SO_4{\cdot}8H_2O$ (1.536 g, 9.6 mmol) were dissolved in deionized water (170 mL) to get a solution. Another aqueous solution (80 mL) prepared by dissolving $MnSO_4{\cdot}H_2O$ (17.600 g, 104.0 mmol) and $FeSO_4{\cdot}7H_2O$ (2.432 g, 8.8 mmol) was added dropwise into the above-mentioned solution to get brown slurry. The slurry was subsequently refluxed at 100 °C in a 1000 mL round-bottom flask for 24 h. The resulting solid was washed with deionized water, filtered, dried at 110 °C for 12 h, and calcined at 400 °C for 4 h.

To prepare Ag_1/HMO, $AgNO_3$ (0.315 g) was initially dissolved in 30 mL of deionized water to form a solution, to which ammonia (25 wt %) was slowly added under stirring until the solution became transparent. Both the transparent solution and a H_2O_2 solution (30 wt %, 90 mL) were simultaneously added to an aqueous suspension (80 mL) containing HMO NPs (2.000 g) under stirring at 0 °C for 0.5 h. The final suspension was filtered, washed with deionized water, and dried at 80 °C for 12 h to obtain supported Ag NPs (Ag_{NP}/HMO), followed by annealing at 400 °C for 4 h to obtain Ag_1/HMO. The inductively coupled plasma-atomic emission spectroscopy data show that Ag_1/HMO is composed of 10 wt % Ag, 3 wt % K, 44 wt % Mn, 3 wt % Ti, 3 wt % V, 3 wt % Fe, and 1 wt % Mo. Ag_2SO_4 powder and metal Ag particles (10 μm in size) were purchased from Aladdin for the X-ray photoelectron spectra (XPS) measurements. Other materials and chemicals were commercially available and were used as received.

Material Characterization. Synchrotron X-ray diffraction (SXRD) patterns were performed at BL14B of the Shanghai Synchrotron Radiation Facility (SSRF) at a wavelength of 1.2398 Å. The beam was monochromatized using Si (111), and a Rh/Si mirror was used for the beam focusing to a size of around 0.5 × 0.5 mm^2.

High-resolution transmission electron microscopy (HRTEM) images, and scanning TEM (STEM) with energy dispersive X-ray spectroscopy (EDS) mapping obtained with a JEOL JEM-2100F field-emission gun transmission electron microscope operating at an accelerating voltage of 200 kV and equipped with an ultrahigh resolution pole-piece that provides a

DOI: 10.1021/acs.est.6b04340
Environ. Sci. Technol. 2017, 51, 2304−2311

point-resolution better than 0.19 nm. Fine powders of the materials were dispersed in ethanol, sonified, and sprayed on a carbon coated copper grid, and then allowed to air-dry for imaging.

X-ray absorption near-edge structure (XANES) spectra and extended X-ray absorption fine structure (EXAFS) spectra were measured at the Ag *K*-edge at BL14W of the SSRF with an electron beam energy of 3.5 GeV and a ring current of 200−300 mA. Data were collected with a fixed exit monochromator using two flat Si(311) crystals. The XANES spectra were acquired at an energy step of 0.5 eV. The EXAFS spectra were collected in a transmission mode using ion chambers filled with N_2. The raw data were analyzed using the IFEFFIT 1.2.11 software package.

H_2 temperature-programmed reduction of H_2 (H_2-TPR) experiments were performed on a 2920 adsorption instrument (Micromeritics, USA) with a thermal conductivity detector (TCD) to monitor the consumed H_2. H_2-TPR was conducted at 10 °C min^{-1} in a 50 mL min^{-1} flow of 5 vol % H_2 in Ar.

Core-level XPS spectra were collected using the Kratos Axis Ultra-DLD system with a charge neutralizer and a 150 W Al (Monochromatized) X-ray gun (1486.6 eV) with an energy resolution of ∼0.15 eV. The spectrometer was equipped with a delay-line detector. Spectra were acquired at normal emission with a passing energy of 40 eV. XPS were referenced to the C 1*s* peak at the binding energy (BE) of 284.6 eV. Metal Ag particles, as the reference of metal Ag, was cleaned using the Ar ion sputtering gun operating at 4 keV and 15 mA before the measurement. Data analysis and processing were undertaken using the XPSPeak4.1 software with the Shirley type background. Valence-band XPS spectra were obtained at BL 4B9B in the Beijing Synchrotron Radiation Facility (BSRF) at a photon energy of 100 eV. All the data were recorded in an ultrahigh vacuum chamber equipped with a VG Scienta R4000 electron energy analyzer with a base pressure of ∼4×10^{-11} mbar at room temperature. BE of these valence-band spectra were calibrated with respect to the Au $4f_{7/2}$ (BE = 84 eV) featured from a clean gold foil attached to the manipulator.

Catalytic Evaluation. The complete oxidation of benzene was performed in a fixed-bed quartz reactor under atmospheric pressure. A certain amount of the catalyst (40−60 mesh) was loaded for each run with a total flow rate of 100 mL min^{-1}. The feed gas was composed of 200 ppm benzene, 20 vol % O_2, and balanced N_2. Effluents from the reactor were analyzed with an online Agilent 7890A gas chromatograph equipped with TCD and FID detectors. Surface reaction kinetics of benzene oxidation was studied at 180 °C over Ag_1/HMO and HMO by controlling conversions of benzene less than 20%. Benzene concentrations were controlled in the range of 50−200 ppm and the corresponding O_2 concentration in the range of 7000−17500 ppm. The data were recorded up to the steady state for each run.

Density Function Theory (DFT) Calculations. All of the configurations were implemented in the Vienna *ab initio* Simulation Package (VASP). The generalized-gradient approximation[29] with Perdew−Burke−Ernzerh (PBE)[30] functional was performed in density functional theory calculations. The energy cutoff for the plane waves was set to 450 eV. In the calculation of Ag bulk, the lattice constants for a conventional face-centered cubic cell were 4.086 Å × 4.086 Å × 4.086 Å, and 2 × 2 × 2 monkhorst-pack grid was used in the k-point sampling for the geometry optimization of Ag bulk. For Ag_1/HMO, lattice constants were set to be 9.815 Å × 9.815 Å × 2.847 Å, and 2 × 2 × 1 monkhorst-pack grid was used in the k-point sampling for the geometry optimization.

RESULTS AND DISCUSSION

HMO usually grows along the ⟨001⟩ direction to form a rod-shaped morphology with a high aspect ratio owing to the low surface energy of the {001} facets.[31−33] To improve the ability toward activating oxygen, we synthesized HMO NPs with an average size of 4 nm (Figure 1a). Figure 1b shows an HRTEM image of a typical HMO NP from the ⟨001⟩ direction. Obviously, HMO is constructed by four {110} facets with intersecting lattice angles of 90°. According to another lattice angle of 45° between the (040) plane and the (110) side-facets and the SXRD pattern of HMO in Figure S1, it is convincing that HMO surfaces comprise four {110} facets and two {001} top-facets.

Ag_1/HMO was synthesized by the thermal diffusion process (also called anti-Ostwald ripening method[31,34]). First, Ag NPs with a truncated octahedron shape (Figure 1c) were deposited on HMO surfaces to obtain Ag_{NP}/HMO (Figure 1c,d), as confirmed by the SXRD pattern of Ag_{NP}/HMO (Figure S1). After annealing, the SXRD peaks due to Ag NPs vanished, and no new peaks due to Ag species appeared in the SXRD pattern of Ag_1/HMO (Figure S1), while the hollandite crystal structure was preserved except for slight modifications,[35] reflecting that Ag atoms are highly dispersed on HMO.[31,36] The highly dispersed Ag atoms can be directly imaged by TEM (Figures 1e and S2). The HRTEM image in an inset of Figure 1e was slightly smoothed after Fourier transform (FT) filtering to increase the signal-to-noise ratio. To illustrate the contrast of Ag and Mn, we constructed the intensity surface plot shown in Figure 1f. The intensity variations of Ag atoms are easily distinguishable from those of Mn and O atoms, clearly demonstrating that the bright atomic dots with a highly dense array in the HRTEM image are Ag atoms. The distance between near neighbor Ag atoms is ∼5.7 Å,[27] twice the length of the Ag−Ag bonds (∼2.88 Å) in bulk Ag (Table S1), reflecting that the Ag atoms anchored on HMO surfaces are mainly at the isolated states.

Figure 2a shows the FT amplitudes of the $\chi(R)$ k^2-weighted EXAFS data at the Ag *K*-edge of the samples to determine the local structure of the Ag atoms. The structural parameters obtained by fitting the spectra with theoretical models are summarized in Table S1.[36] The curve-fitting of the *R*-space and the inverse FT spectra are given in Figure S3. The FT amplitude of the EXAFS spectrum of Ag_1/HMO in 2.8−3.0 Å owing to the scattering between the Ag atoms is absent, indicating the isolated states of the Ag atoms. The first two shells with distances of ∼2.35 and ∼2.62 Å and coordination numbers of 4 and 1, implying that the isolated Ag atoms are anchored on HMO surfaces, are consistent with the HRTEM observation (Figure 1e).

The metallic states of Ag atoms are preserved when isolated Ag atoms are formed on HMO surfaces, as shown in the XANES spectra in Figure 2b. Ag_1/HMO exhibits a sharp resonance (white-line) in absorption coefficient, and the absorption threshold energy (E_0) ∼ 25514 eV is close to the E_0 value of Ag foil and higher than the E_0 of Ag_2O,[31,37] indicating the presence of $Ag^{\delta+}$ ($0 < \delta < 1$) in Ag_1/HMO. A similar conclusion is reached by analyzing XPS and Ag M_4VV Auger spectra shown in Figure S4. The Ag $3d_{5/2}$ BE value of Ag_1/HMO is 368.1 eV, slightly lower than that (368.4 eV) of metallic Ag and much higher than that (367.4 eV) of Ag_2SO_4.

DOI: 10.1021/acs.est.6b04340
Environ. Sci. Technol. 2017, 51, 2304−2311

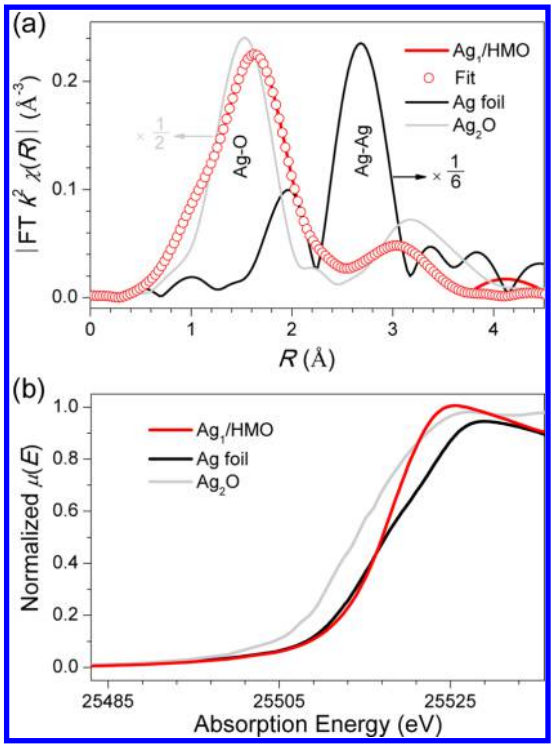

Figure 2. (a) $\chi(R)$ k^2-weighted FT EXAFS spectra of Ag_1/HMO, Ag foil, and Ag_2O. (b) Ag *K*-edge XANES spectra of Ag_1/HMO, Ag foil, and Ag_2O.

The corresponding Ag M_4VV Auger spectra also indicate the metallic Ag state of Ag_1/HMO.[27]

Ag_1/HMO synthesized at an elevated temperature of 400 °C was suitably applied in high-temperature oxidation of some formidable VOCs such as benzene. Figure 3 shows the conversion of benzene (X_{C6H6}) as a function of reaction temperature. Ag_1/HMO shows excellent catalytic activity at low temperature, and the temperature required for 50% X_{C6H6} (T_{50}) is 170 °C at a gaseous hourly space velocity (GHSV) of 23 000 h^{-1}, lower than a reported T_{50} value (190 °C) over Pt/Al_2O_3 or Pd/Al_2O_3 at a similar GHSV.[38] Even at a GHSV as high as 92 000 h^{-1}, the T_{50} value is only 200 °C. To shed light on the high activity of Ag_1/HMO, Arrhenius plots were depicted in Figure S5. The apparent activation energy (E_a) is ~58 kJ mol^{-1}, much lower than those (E_a = 90–100 kJ mol^{-1}) over Pt/Al_2O_3 or Pd/Al_2O_3.[38,39] This implies that the reaction mechanism of benzene oxidation over Ag_1/HMO possibly differs from that over Pt/Al_2O_3 and Pd/Al_2O_3. For comparison, HMO gives a T_{50} of 300 °C, much higher than that of Ag_1/HMO. Furthermore, the oxidation state of Mn of HMO almost remains unchanged after the Ag loading (Figure S6). The data above demonstrate that the Ag atoms are catalytic sites and HMO mainly functions as a support for Ag_1/HMO in benzene oxidation.

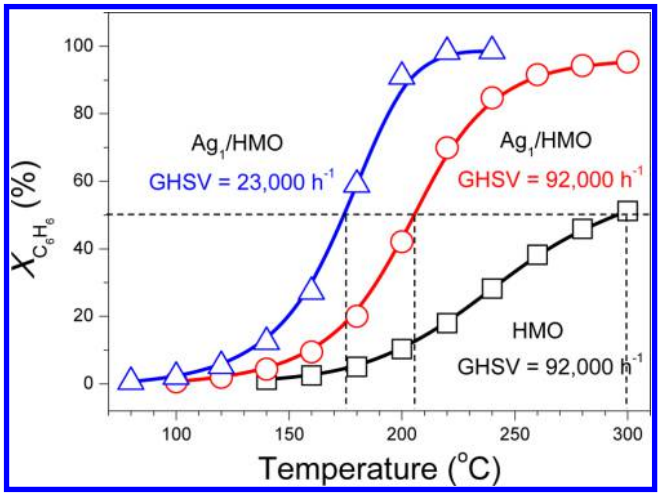

Figure 3. Conversion of benzene (X_{C6H6}) as a function of temperature over Ag_1/HMO at different gaseous hourly space velocities (GHSVs) and X_{C6H6} of HMO at a GHSV of 92 000 h^{-1} are also given for comparison. Reaction conditions: benzene, 200 ppm; O_2, 20% and balanced by N_2; flow rate, 100 mL min^{-1}.

To explain the high activity of Ag_1/HMO, the reaction kinetics of benzene oxidation at 180 °C over Ag_1/HMO and HMO was studied. The reaction orders (k_r) were achieved by keeping X_{C6H6} lower than 20%.[38] The k_r of benzene and O_2 for Ag_1/HMO are ~0.9 and ~0.7, respectively (Figure 4), much

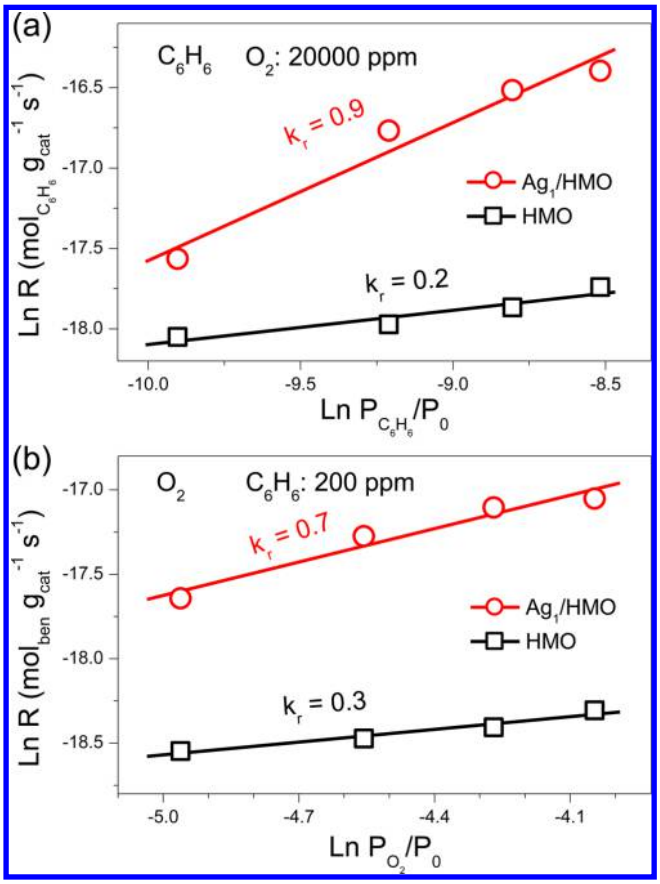

Figure 4. Reaction orders (k_r) for benzene (a) and O_2 (b) over Ag_1/HMO and HMO at the reaction temperature of 180 °C.

higher than the corresponding k_r (only ~0.2 or ~0.3) for HMO. Therefore, benzene oxidation over Ag_1/HMO does not follow the Eley–Rideal mechanism, in which one adsorbed reactant molecule reacts with another gaseous reactant molecule.[40] The Langmuir-Hinshelwood (L-H) or M-K mechanism may be more suitable to describe benzene oxidation over Ag_1/HMO. The L-H mechanism seems to be satisfactory for Pt or Pd NP catalysts supported on nonreducible oxides such as Al_2O_3.[38,39] These supports are often regarded as "inert supports"[41] because of the absence of surface active lattice

DOI: 10.1021/acs.est.6b04340
Environ. Sci. Technol. 2017, 51, 2304–2311

oxygen ions. Two active sites required for the L-H mechanism (responsible for adsorbing benzene and O_2) are provided by Pt or Pd atoms of metal NPs,[42] where the k_r with respect to benzene is always positive in the 0−1 range, while the reaction order for O_2 often approaches zero or becomes negative.[38,39,42,43]

The M-K mechanism, often applied to catalytic oxidation over reducible metal oxides, still holds true for catalytic oxidation over metal supported on reducible metal oxides.[31,44] This mechanism involves a two-stage redox cycle: (i) VOCs are oxidized by surface lattice oxygen of catalysts at the vicinity of catalytically active sites (CASs), producing oxygen vacancies; (ii) the partially reduced catalysts are oxidized by gaseous oxygen, replenishing oxygen vacancies. For Ag-HMO catalysts, the M-K mechanism is valid for describing oxidation reactions such as CO and formaldehyde oxidation due to the excellent redox property of HMO.[31,45] As for Ag_1/HMO in the current work, the CASs only comprise individual Ag atoms with a size of 0.29 nm. These individual Ag atoms cannot adsorb one benzene molecule (with a size of 0.55 nm)[46] and one O_2 molecule (0.33 nm in size) simultaneously.[47] Taking k = 0.7 with respect to O_2 and "active" reducible manganese oxide support[41] into account, benzene oxidation over Ag_1/HMO could be described by the M-K mechanism, where the activity of surface lattice oxygen and activation of gaseous oxygen play important roles in determining the activity.

The activity of surface lattice oxygen of Ag_1/HMO was studied by H_2-TPR. As shown in Figure 5a, the reduction of HMO starts at ∼150 °C, and a weak reduction peak at 225 °C can be ascribed to the surface oxygen species, merely accounting for ∼3% of the total oxygen species of HMO, indicating that only a minority of oxygen is active at this temperature. After Ag is loaded onto HMO, the reducibility of HMO is drastically improved, and a very strong reduction peak shifts down to the low temperature range and centers at 90 °C. This reduction peak can be assigned to the surface lattice oxygen species in the vicinity of the isolated Ag atoms.[19] Thus, ∼28% of the Ag_1/HMO oxygen are surface oxygen lattice species calculated by curve-fitting the H_2-TPR profile. These species can participate in benzene oxidation.

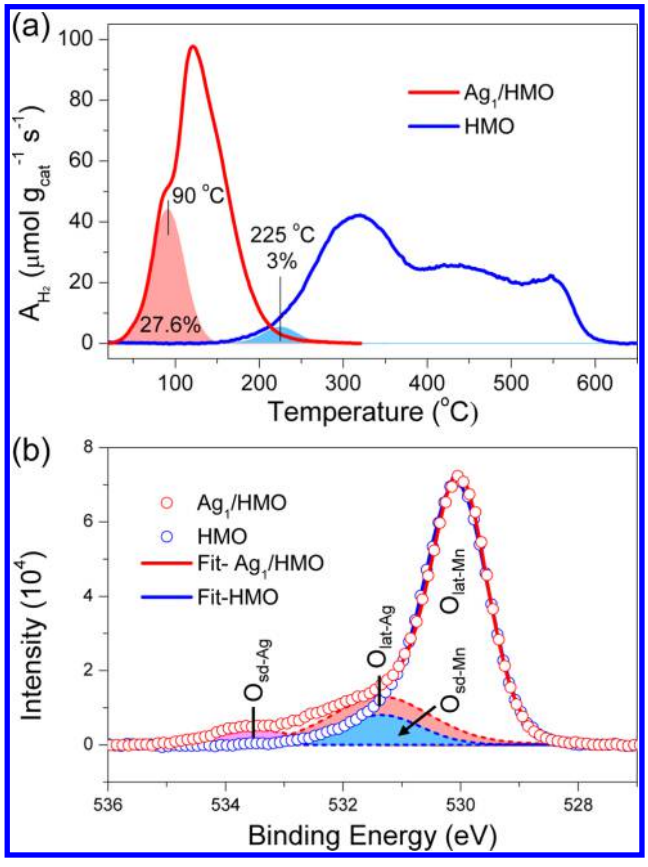

Figure 5. (a) H_2-TPR profiles and (b) O 1*s* XPS of Ag_1/HMO and HMO.

According to the calculated results (Supporting Discussion 1) and considering the interatomic distance between the neighbor Ag atoms of 5.7 Å (Figure 1e), ∼2.5 Å surface layer of Ag_1/HMO is active. We recently investigated the activity of surface lattice oxygen of isolated Ag atoms supported on HMO rods and found that ∼12 (sub)surface active lattice oxygen atoms in the vicinity of Ag atoms are available for oxidation reactions by using a temporal analysis of products reactor at 70 °C.[34] This means that lattice oxygen atoms in a ∼3.6 Å radius zone around Ag atoms are accessible for oxidation reactions, and these lattice oxygen atoms can be replenished by gaseous O_2 upon activation. In this work, benzene oxidation occurs at reaction temperatures higher than 70 °C, and thus, more lattice oxygen atoms of Ag_1/HMO should be involved in the reaction. Therefore, a majority of the active surface lattice oxygen ions are enough to satisfy the requirement for benzene oxidation.

As the activity of lattice oxygen may be directly related to their electronic features, we carried out XPS measurements. Figure 5b displays the O 1*s* XPS of Ag_1/HMO and HMO. The O 1*s* XPS data of HMO indicate the presence of two kinds of oxygen species after curve-fitting: one peak with a BE centered at 530 eV can be ascribed to surface lattice oxygen (denoted as $O_{lat\text{-}Mn}$), and the other peak at a higher BE of 532 eV can be ascribed to surface defect oxygen bound to surface Mn ions ($O_{sd\text{-}Mn}$).[48] After loading Ag onto HMO, the electronic states of $O_{lat\text{-}Mn}$ of HMO almost remain unchanged, and the XPS peak appears at BE of 530 eV. Note that two kinds of new oxygen species appear at a higher BE range of 531−535 eV. On the basis of the surface structure of Ag_1/HMO (Figures 1 and 2), the peak at 532.4 eV can be ascribed to surface lattice oxygen bound to Ag atoms ($O_{lat\text{-}Ag}$).[49,50] The peak at the highest BE of 533.5 eV might be due to surface defect oxygen species adsorbed on the Ag atoms ($O_{sd\text{-}Ag}$), because the peak is absent for the pure HMO. Both $O_{sd\text{-}Ag}$ and $O_{lat\text{-}Ag}$ with BEs higher than $O_{lat\text{-}Mn}$ indicate that the oxygen species around Ag atoms have an electronic density lower than those bound to Mn, thus allowing them to easily accept electrons from benzene via the reaction: $C_6H_6 + 7.5O_2 \rightarrow 6CO_2 + 3H_2O$. The highly active oxygen species of Ag_1/HMO have strong oxidization ability (Figure 5a), increasing the reaction order with respect to C_6H_6 (Figure 4a), and thereby enhancing the activity of benzene oxidation.

The M-K mechanism also involves the activation of gaseous oxygen to replenish the surface oxygen defects produced by benzene oxidation. The activation of O_2 can be investigated by using O_2-TPD[51] or by studying the nature of CASs,[34,52] because the ability for activating O_2 is essentially associated with the electronic states or the *d*-orbital centroid of CASs. A correlation between the *d*-band centroid of metal surfaces and activation of O_2 was established by Hammer and Nørskov.[52] In particular, the upshifted *d*-band centroid of Ag is favorable for dissociation of O_2 by charge transfer from the Ag 4*d* orbitals to antibonding π^* orbitals of O_2.[53,54] Hence, to understand the

DOI: 10.1021/acs.est.6b04340
Environ. Sci. Technol. 2017, 51, 2304−2311

activation ability toward O_2, we carried out the valence-band XPS measurements and DFT calculations.

Figure 6a shows the XPS of the valence band of Ag_1/HMO, HMO, and their difference spectrum, together with bulk Ag as a

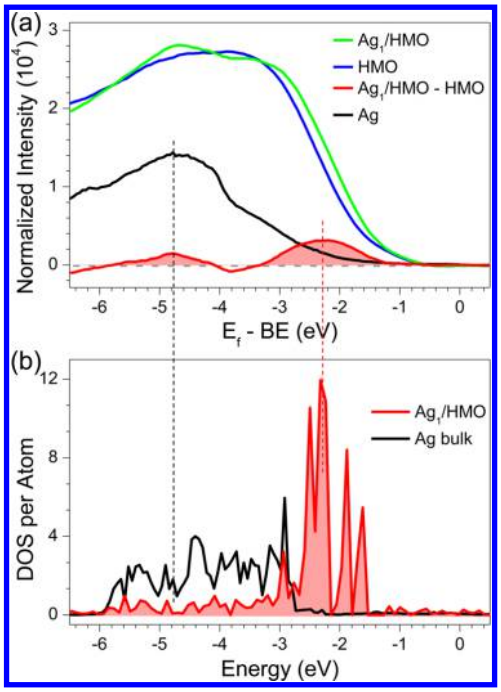

Figure 6. (a) Valence-band XPS of Ag_1/HMO and HMO. (b) Projected DOS of Ag_1/HMO and bulk Ag.

reference. As expected, the Ag *d*-band centroid of bulk Ag is located at ~4.3 eV.[55] The Ag *d* orbital centroid of the isolated Ag atoms of Ag_1/HMO distinctly upshifts to a higher energy and is located at ~2.3 eV below the Fermi level (E_f), as seen from the difference spectrum between Ag_1/HMO and HMO. Indeed, H_2 is an effective electronic descriptor for the shift of the *d* orbital centroid.[53,56] The low-temperature reduction peak of Ag_1/HMO in Figure 4a indicates the upshift of the Ag 4*d* orbital centroid.[34]

We further carried out DFT calculations to confirm the electronic density of states (DOS) of the CASs of Ag_1/HMO. Figure 6b shows the projected DOS of isolated Ag adatoms on HMO surfaces, as constructed according to the TEM images (Figure 1) and EXAFS data (Figure 2). The bulk Ag sample is also shown in Figure 6b for comparison. Still, the Ag *d*-band centroid is at 4.3 eV, consistent with the valence-band XPS in Figure 6a. Note that the Ag *d*-orbital centroid of Ag_1/HMO shifts up to E_f by 2 eV, agreeing fairly with the experimental measurement and the previous report.[54] Consequently, the upshift of the Ag 4*d* orbitals demonstrates that Ag_1/HMO possesses an excellent ability of activating O_2, thus leading to the positive reaction order (k = 0.7) with respect to O_2 in benzene oxidation (Figure 4b).

The results above demonstrate that the isolated Ag adatoms on HMO NPs have an excellent ability toward activating both lattice oxygen and gaseous O_2, resulting in the high catalytic activity in benzene oxidation. In contrast, single Ag adatoms on HMO rods only give ~3% active surface oxygen according to the H_2-TPR analysis in our recent report,[19] and presumably, such a great amount of active surface lattice oxygen species of Ag_1/HMO is intimately associated with the HMO size or a support nanoscale effect (Figure 1a,b). Similarly, Libuda and co-workers reported that the presence of nanostructured CeO_2 support is required to boost oxygen transfer to Pt NPs,[25] thus strongly enhancing catalytic activity.

In conclusion, we synthesized Ag_1/HMO by depositing individual Ag atoms on the 4 nm HMO nanoparticles. The isolated Ag atoms were anchored on the surface cavities of HMO serving as the catalytically active sites in benzene oxidation. Ag_1/HMO showed high catalytic activity, and the complete oxidation of benzene was achieved at 220 °C at a high GHSV of 23 000 h^{-1}. The reaction orders with respect to benzene and O_2 were determined to be 0.9 and 0.7, respectively, indicating that benzene oxidation followed the M-K mechanism. HMO NPs were demonstrated to be favorable for producing a great amount of active surface lattice oxygen after the atomic Ag loading, and the upshifted 4*d* orbitals of the Ag adatoms facilitated the activation of gaseous oxygen. Our findings enable us to understand the enhanced catalytic performance in benzene oxidation over metal catalysts with nanosized supports from the oxygen activation point of view and to rationally design efficient metal-oxide catalysts for the abatement of VOCs.

■ ASSOCIATED CONTENT

Supporting Information

The Supporting Information is available free of charge on the ACS Publications website at DOI: 10.1021/acs.est.6b04340.

Calculation of the depth of active surface layer; EXAFS analysis results; SXRD patterns of the samples; HAADF-STEM image and EDS mappings; Ag *K*-edge $\chi(R)$ k^2-weighted *R*-space and inverse FT spectra; Ag 3*d* XPS and Ag MVV spectra; Arrhenius plot; Mn 2p XPS (PDF)

■ AUTHOR INFORMATION

Corresponding Author

*Phone: +86-21-65642997; fax: +86-21-65643597; e-mail: tangxf@fudan.edu.cn.

ORCID

Xingfu Tang: 0000-0002-0746-1294

Notes

The authors declare no competing financial interest.

■ ACKNOWLEDGMENTS

This work was financially supported by the NSFC (21277032 and 21477023) and the STCSM (14JC1400400). The SXRD and X-ray absorption spectroscopy measurements were conducted at the SSRF. The valence-band XPS spectroscopy measurements were conducted at the BSRF.

■ REFERENCES

(1) Einaga, H.; Futamura, S.; Ibusuki, T. Complete oxidation of benzene in gas phase by platinized titania photocatalysts. *Environ. Sci. Technol.* **2001**, *35* (9), 1880−1884.

(2) Li, T. Y.; Chiang, S. J.; Liaw, B. J.; Chen, Y. Z. Catalytic oxidation of benzene over $CuO/Ce_{1-x}Mn_xO_2$ catalysts. *Appl. Catal., B* **2011**, *103* (1−2), 143−148.

(3) *Integrated Risk Information System (IRIS) on Benzene*; U.S. Environmental Protection Agency: Washington, DC, 2006.

(4) Finlayson-Pitts, B. J.; Pitts, J. N., Jr. Tropospheric air pollution: Ozone, airborne toxics, polycyclic aromatic hydrocarbons, and particles. *Science* **1997**, *276* (5315), 1045−1051.

(5) Volkamer, R.; Jimenez, J. L.; Martini, F. S.; Dzepina, K.; Zhang, Q.; Salcedo, D.; Molina, L. T.; Worsnop, D. R.; Molina, M. J.

DOI: 10.1021/acs.est.6b04340
Environ. Sci. Technol. 2017, 51, 2304−2311

Secondary organic aerosol formation from anthropogenic air pollution: Rapid and higher than expected. *Geophys. Res. Lett.* **2006**, *33* (17), L17811.
(6) Luo, Y.; Wang, K.; Chen, Q.; Xu, Y.; Xue, H.; Qian, Q. Preparation and characterization of electrospun $La_{1-x}Ce_xCoO_\delta$: Application to catalytic oxidation of benzene. *J. Hazard. Mater.* **2015**, *296*, 17−22.
(7) Genuino, H. C.; Dharmarathna, S.; Njagi, E. C.; Mei, M. C.; Suib, S. L. Gas-phase total oxidation of benzene, toluene, ethylbenzene, and xylenes using shape-selective manganese oxide and copper manganese oxide catalysts. *J. Phys. Chem. C* **2012**, *116* (22), 12066−12078.
(8) Lai, S. Y.; Qiu, Y.; Wang, S. Effects of the structure of ceria on the activity of gold/ceria catalysts for the oxidation of carbon monoxide and benzene. *J. Catal.* **2006**, *237* (2), 303−313.
(9) He, C.; Li, J.; Li, P.; Cheng, J.; Hao, Z.; Xu, Z. Comprehensive investigation of Pd/ZSM-5/MCM-48 composite catalysts with enhanced activity and stability for benzene oxidation. *Appl. Catal., B* **2010**, *96* (3), 466−475.
(10) Li, J. J.; Xu, X. Y.; Jiang, Z.; Hao, Z. P.; Hu, C. Nanoporous silica-supported nanometric palladium: Synthesis, characterization, and catalytic deep oxidation of benzene. *Environ. Sci. Technol.* **2005**, *39* (5), 1319−1323.
(11) Luo, J.; Zhang, Q.; Huang, A.; Suib, S. L. Total oxidation of volatile organic compounds with hydrophobic cryptomelane-type octahedral molecular sieves. *Microporous Mesoporous Mater.* **2000**, *35*−*36*, 209−217.
(12) Hou, J.; Liu, L.; Li, Y.; Mao, M.; Lv, H.; Zhao, X. Tuning the K^+ concentration in the tunnel of OMS-2 nanorods leads to a significant enhancement of the catalytic activity for benzene oxidation. *Environ. Sci. Technol.* **2013**, *47* (23), 13730−13736.
(13) Debecker, D. P.; Delaigle, R.; Bouchmella, K.; Eloy, P.; Gaigneaux, E. M.; Mutin, P. H. Total oxidation of benzene and chlorobenzene with MoO_3- and WO_3-promoted V_2O_5/TiO_2 catalysts prepared by a nonhydrolytic sol−gel route. *Catal. Today* **2010**, *157* (1), 125−130.
(14) Delaigle, R.; Joseph, M. M.; Debecker, D. P.; Eloy, P.; Gaigneaux, E. M. An alternative method for the incorporation of silver in Ag-VO_x/TiO_2 catalysts for the total oxidation of benzene. *Top. Catal.* **2013**, *56* (18−20), 1867−1874.
(15) Debecker, D. P.; Faure, C.; Meyre, M. E.; Derré, A.; Gaigneaux, E. M. A new bio-inspired route to metal-nanoparticle-based heterogeneous catalysts. *Small* **2008**, *4* (10), 1806−1812.
(16) Santos, V. P.; Pereira, M. F. R.; Órfão, J. J. M.; Figueiredo, J. L. The role of lattice oxygen on the activity of manganese oxides towards the oxidation of volatile organic compounds. *Appl. Catal., B* **2010**, *99* (1), 353−363.
(17) Kim, S. C.; Shim, W. G. Catalytic combustion of VOCs over a series of manganese oxide catalysts. *Appl. Catal., B* **2010**, *98* (3), 180−185.
(18) Wang, R.; Li, J. Effects of precursor and sulfation on OMS-2 catalyst for oxidation of ethanol and acetaldehyde at low temperatures. *Environ. Sci. Technol.* **2010**, *44* (11), 4282−4287.
(19) Hu, P.; Amghouz, Z.; Huang, Z.; Xu, F.; Chen, Y.; Tang, X. Surface-confined atomic silver centers catalyzing formaldehyde oxidation. *Environ. Sci. Technol.* **2015**, *49* (4), 2384−2390.
(20) Xu, F.; Huang, Z.; Hu, P.; Chen, Y.; Zheng, L.; Gao, J.; Tang, X. The promotion effect of isolated potassium atoms with hybridized orbitals in catalytic oxidation. *Chem. Commun.* **2015**, *51* (48), 9888.
(21) Huang, Y.; Zhang, M.; Zhao, L.; Feng, J.; Wu, D.; Ren, B.; Tian, Z. Activation of oxygen on gold and silver nanoparticles assisted by surface plasmon resonances. *Angew. Chem., Int. Ed.* **2014**, *53* (9), 2353−2357.
(22) Lei, Y.; Mehmood, F.; Lee, S.; Greeley, J.; Lee, B.; Seifert, S.; Winans, R. E.; Elam, J. W.; Meyer, R. J.; Redfern, P. C.; Teschner, D.; Schlögl, R.; Pellin, M. J.; Curtiss, L. A.; Vajda, S. Increased silver activity for direct propylene epoxidation via subnanometer size effects. *Science* **2010**, *328* (5975), 224−228.
(23) Chen, J.; Tang, X.; Liu, J.; Zhan, S.; Li, J.; Huang, X.; Shen, W. Synthesis and characterization of Ag-hollandite nanofibers and its catalytic application in ethanol oxidation. *Chem. Mater.* **2007**, *19* (17), 4292−4299.
(24) Xia, G.; Yin, Y.; Willis, W. S.; Wang, J.; Suib, S. L. Efficient stable catalysts for low temperature carbon monoxide oxidation. *J. Catal.* **1999**, *185* (1), 91−105.
(25) Vayssilov, G. N.; Lykhach, Y.; Migani, A.; Staudt, T.; Petrova, G. P.; Tsud, N.; Skála, T.; Bruix, A.; Illas, F.; Prince, K. C.; Matolín, V.; Neyman, K. M.; Libuda, J. Support nanostructure boosts oxygen transfer to catalytically active platinum nanoparticles. *Nat. Mater.* **2011**, *10* (4), 310−315.
(26) Chen, Y.; Huang, Z.; Hu, P.; Chen, J.; Tang, X. Improved performance of supported single-atom catalysts via increased surface active sites. *Catal. Commun.* **2016**, *75*, 74−77.
(27) Chen, Y.; Kasama, T.; Huang, Z.; Hu, P.; Chen, J.; Liu, X.; Tang, X. Highly dense isolated metal atom catalytic sites: Dynamic formation and in situ observations. *Chem. - Eur. J.* **2015**, *21* (48), 17397−17402.
(28) King'ondu, C. K.; Opembe, N.; Chen, C.; Ngala, K.; Huang, H.; Iyer, A.; Garcés, H. F.; Suib, S. L. Manganese oxide octahedral molecular sieves (OMS-2) multiple framework substitutions: A new route to OMS-2 particle size and morphology control. *Adv. Funct. Mater.* **2011**, *21* (2), 312−323.
(29) Kresse, G.; Joubert, D. From ultrasoft pseudopotentials to the projector augmented-wave method. *Phys. Rev. B: Condens. Matter Mater. Phys.* **1999**, *59* (3), 1758−1775.
(30) Perdew, J. P.; Burke, K.; Ernzerhof, M. Generalized gradient approximation made simple. *Phys. Rev. Lett.* **1996**, *77* (18), 3865−3868.
(31) Huang, Z.; Gu, X.; Cao, Q.; Hu, P.; Hao, J.; Li, J.; Tang, X. Catalytically active single-atom sites fabricated from silver particles. *Angew. Chem., Int. Ed.* **2012**, *51* (17), 4198−4203.
(32) Espinal, A. E.; Zhang, L. C.; Chen, C. H.; Morey, A.; Nie, Y. F.; Espinal, L.; Wells, B. O.; Joesten, R.; Aindow, M.; Suib, S. L. Nanostructured arrays of semiconducting octahedral molecular sieves by pulsed-laser deposition. *Nat. Mater.* **2010**, *9* (1), 54−59.
(33) Chen, C. H.; Jin, L.; Espinal, A. E.; Firliet, B. T.; Xu, L.; Aindow, M.; Joesten, R.; Suib, S. L. Heteroepitaxial growth of nanoscale oxide shell/fiber superstructures by mild hydrothermal processes. *Small* **2010**, *6* (9), 988−992.
(34) Hu, P.; Huang, Z.; Amghouz, Z.; Makkee, M.; Xu, F.; Kapteijn, F.; Dikhtiarenko, A.; Chen, Y.; Gu, X.; Tang, X. Electronic metal-support interactions in single-atom catalysts. *Angew. Chem., Int. Ed.* **2014**, *53* (13), 3418−3421.
(35) Li, L. Y.; King, D. L. Synthesis and characterization of silver hollandite and its application in emission control. *Chem. Mater.* **2005**, *17* (17), 4335−4343.
(36) Chang, F. M.; Jansen, M. $Ag_{1.8}Mn_8O_{16}$: Square planar coordinated $Ag^{\oplus}$ ions in the channels of a novel hollandite variant. *Angew. Chem., Int. Ed. Engl.* **1984**, *23* (11), 906−907.
(37) Kolobov, A. V.; Rogalev, A.; Wilhelm, F.; Jaouen, N.; Shima, T.; Tominaga, J. Thermal decomposition of a thin AgO_x layer generating optical near-field. *Appl. Phys. Lett.* **2004**, *84* (10), 1641−1643.
(38) Papaefthimiou, P.; Ioannides, T.; Verykios, X. E. Combustion of non-halogenated volatile organic compounds over group VIII metal catalysts. *Appl. Catal., B* **1997**, *13* (3), 175−184.
(39) Garetto, T. F.; Apesteguıa, C. R. Structure sensitivity and in situ activation of benzene combustion on Pt/Al_2O_3 catalysts. *Appl. Catal., B* **2001**, *32* (1), 83−94.
(40) Ordóñez, S.; Bello, L.; Sastre, H.; Rosal, R.; Díez, F. V. Kinetics of the deep oxidation of benzene, toluene, *n*-hexane and their binary mixtures over a platinum on γ-alumina catalyst. *Appl. Catal., B* **2002**, *38* (2), 139−149.
(41) Schubert, M. M.; Hackenberg, S.; Van Veen, A. C.; Muhler, M.; Plzak, V.; Behm, R. J. CO oxidation over supported gold catalysts—"Inert" and "active" support materials and their role for the oxygen supply during reaction. *J. Catal.* **2001**, *197* (1), 113−122.
(42) Barresi, A. A.; Baldi, G. Deep catalytic oxidation of aromatic hydrocarbon mixtures: Reciprocal inhibition effects and kinetics. *Ind. Eng. Chem. Res.* **1994**, *33* (12), 2964−2974.

DOI: 10.1021/acs.est.6b04340
Environ. Sci. Technol. 2017, 51, 2304−2311

(43) Liotta, L. F. Catalytic oxidation of volatile organic compounds on supported noble metals. *Appl. Catal., B* **2010**, *100* (3), 403−412.
(44) Widmann, D.; Behm, R. J. Active oxygen on a Au/TiO_2 catalyst: Formation, stability, and CO oxidation activity. *Angew. Chem., Int. Ed.* **2011**, *50* (43), 10241−10245.
(45) Özacar, M.; Poyraz, A. S.; Genuino, H. C.; Kuo, C.; Meng, Y.; Suib, S. L. Influence of silver on the catalytic properties of the cryptomelane and Ag-hollandite types manganese oxides OMS-2 in the low-temperature CO oxidation. *Appl. Catal., A* **2013**, *462*−*463*, 64−74.
(46) Cyrański, M. K. Energetic aspects of cyclic pi-electron delocalization: Evaluation of the methods of estimating aromatic stabilization energies. *Chem. Rev.* **2005**, *105*, 3773−3811.
(47) Outka, D. A.; Stöhr, J.; Jark, W.; Stevens, P.; Solomon, J.; Madix, R. J. Orientation and bond length of molecular oxygen on Ag (110) and Pt (111): A near-edge X-ray-absorption fine-structure study. *Phys. Rev. B: Condens. Matter Mater. Phys.* **1987**, *35* (8), 4119−4122.
(48) Hu, P.; Huang, Z.; Hua, W.; Gu, X.; Tang, X. Effect of H_2O on catalytic performance of manganese oxides in NO reduction by NH_3. *Appl. Catal., A* **2012**, *437*−*438*, 139−148.
(49) Spahr, M. E.; Novák, P.; Schnyder, B.; Haas, O.; Nesper, R. Characterization of layered lithium nickel manganese oxides synthesized by a novel oxidative coprecipitation method and their electrochemical performance as lithium insertion electrode materials. *J. Electrochem. Soc.* **1998**, *145* (4), 1113−1121.
(50) Shaju, K. M.; Subba Rao, G. V.; Chowdari, B. V. R. Performance of layered $Li(Ni_{1/3}Co_{1/3}Mn_{1/3})O_2$ as cathode for Li-ion batteries. *Electrochim. Acta* **2002**, *48* (2), 145−151.
(51) Chen, J.; Li, J.; Li, H.; Huang, X.; Shen, W. Facile synthesis of Ag-OMS-2 nanorods and their catalytic applications in CO oxidation. *Microporous Mesoporous Mater.* **2008**, *116* (1), 586−592.
(52) Hammer, B.; Nørskov, J. K. Theoretical surface science and catalysis—calculations and concepts. *Adv. Catal.* **2000**, *45*, 71−129.
(53) Xu, Y.; Greeley, J.; Mavrikakis, M. Effect of subsurface oxygen on the reactivity of the Ag (111) surface. *J. Am. Chem. Soc.* **2005**, *127* (37), 12823−12827.
(54) Chen, Y.; Huang, Z.; Zhou, M.; Hu, P.; Du, C.; Kong, L.; Chen, J.; Tang, X. The active sites of supported silver particle catalysts in formaldehyde oxidation. *Chem. Commun.* **2016**, *52* (65), 9996−9999.
(55) Ruban, A.; Hammer, B.; Stoltze, P.; Skriver, H. L.; Nørskov, J. K. Surface electronic structure and reactivity of transition and noble metals. *J. Mol. Catal. A: Chem.* **1997**, *115* (3), 421−429.
(56) Acerbi, N.; Tsang, S. C. E.; Jones, G.; Golunski, S.; Collier, P. Rationalization of interactions in precious metal/ceria catalysts using the *d*-band center model. *Angew. Chem., Int. Ed.* **2013**, *52* (30), 7737−7741.

DOI: 10.1021/acs.est.6b04340
Environ. Sci. Technol. 2017, 51, 2304−2311